INORGANIC CHEMISTRY
FRONTIERS

RESEARCH ARTICLE

View Article Online
View Journal | View Issue

Cite this: *Inorg. Chem. Front.*, 2022, **9**, 310

Introducing the penicillamine moiety into a metallopeptide mimicking the NiSOD enzyme: electronic and kinetic effects†

Dóra Bonczidai-Kelemen,[a] Giuseppe Sciortino,[b] Nóra V. May,[c] Eugenio Garribba,[d] István Fábián[a,e] and Norbert Lihi *[a,e]

Multidisciplinary protein design is reported on a novel metallopeptide mimicking the binding loop of nickel containing SOD enzyme (NiSOD). D-Penicillamine, a natural decomposition product of penicillin, was introduced into the peptide chain yielding the H(Pen)DLPCGLY (**wtPen**) peptide. The nickel(II) binding ability of **wtPen** was characterized by thermodynamic (pH-potentiometry), spectroscopic (UV-Vis, CD, MS, NMR) and computational techniques (full DFT and Molecular Dynamics methods). Oxidation of the Ni(II) complex by KO_2 yields a square pyramidal Ni(III) species coordinated by the axial His-N in a well-defined α-helix folding state. The structure of the Ni(III) species was analyzed by EPR spectroscopy and theoretical methods confirming that the donor set involved in the metal ion coordination and the folding state are retained after oxidation. The complex exhibits superior SOD activity which was studied by sequential stopped-flow method. Thorough analysis of the data shows that the Ni(III) species rapidly accumulates in the nickel catalyzed decomposition of superoxide anion. Accordingly, the presence of the penicillamine moiety close to the catalytic center increases the life-time of the Ni(III) transient species. In contrast, Ni(III) exists only at relatively low concentration level in the dismutation reaction catalyzed by the native NiSOD enzyme fragment.

Received 13th August 2021,
Accepted 10th November 2021

DOI: 10.1039/d1qi01025e

rsc.li/frontiers-inorganic

Introduction

Protein design *via* the systematic active site tailoring approach may provide deeper insight into the mechanism of enzyme catalysis. The catalytic reaction can satisfactorily be tuned by exploring the structure–function relationships, the enzyme mechanism in substrate recognition and the kinetic features of the process. Consequently, the controlled design of proteins is a subject of great interest due to their widespread application in industrial biotechnology and chemical synthesis.[1–5] Peptides have also been extensively studied in these reactions due to the easier control of the folding processes compared to proteins.[6] These compounds are easily accessible *via* the routinely used solid phase synthetic methods. Peptides and proteins mimicking the active site of oxygenases have been intensively studied because their controlled regio- and stereochemical features have essential role in the oxygenation processes.[7–9]

Superoxide dismutases (SOD) are a dedicate class of enzyme family which are capable of catalyzing the decomposition of superoxide anion radical in the extracellular matrix.[10–12] The dismutation reaction yields molecular dioxygen and hydrogen peroxide that degrades through various pathways in further reactions catalyzed by catalase or glutathione peroxidase to yield harmful products.[13,14] The absence of these enzymes results in an elevated level of superoxide anion concentration which can cause oxidative stress, the formation of reactive oxygen species (ROS) and extensive cellular damage.[15,16] Several studies have also reported that intensive ROS generation may act as a mediator of a number of inflammatory diseases.[17–20]

Copper/zinc, manganese and iron containing SOD enzymes have been characterized by several methods including structural, equilibrium and computational analysis.[10,21] So far, only limited information is available on the peptide-based controlled design for the relatively novel class of Ni-containing SOD enzymes (NiSOD).[22–25]

[a]*Department of Inorganic and Analytical Chemistry, University of Debrecen, H-4032 Debrecen, Hungary. E-mail: lihi.norbert@science.unideb.hu*
[b]*Institute of Chemical Research of Catalonia (ICIQ), The Barcelona Institute of Technology, 43007 Tarragona, Spain*
[c]*Centre for Structural Science, Research Centre for Natural Sciences, H-1117 Budapest, Hungary*
[d]*Dipartimento di Scienze Mediche, Chirurgiche e Sperimentali, Università di Sassari, I-07100 Sassari, Italy*
[e]*MTA-DE Redox and Homogeneous Catalytic Reaction Mechanisms Research Group, University of Debrecen, H-4032 Debrecen, Hungary*
† Electronic supplementary information (ESI) available: Experimental and computational data. See DOI: 10.1039/d1qi01025e

The NiSOD is expressed by *sodN* gene and found in several *Streptomyces* and cyanobacteria.[26,27] The structure of the NiSOD obtained from X-ray crystallography revealed a unique metal coordination environment, where the first six amino acid residues exhibit a loop. This is the so-called NiSOD binding motif. For the reduced form, nickel(II) is accommodated by the binding of the terminal amino group, the first peptide nitrogen and the thiolate of cysteine resulting in a (5,5)-linked chelate system. This coordination mode is supported by macrochelation due to the distant Cys residue. The (2*N*,2*S*) coordination environment is featured by square planar structure and diamagnetic behavior. The oxidation of the nickel(II) complex yields a paramagnetic nickel(III) species, its formation is being accompanied by an axial ligation which originates from the binding of the imidazole-N of histidine. Earlier studies have demonstrated that the first six amino acid residues (HCDLPC, in the amino acid one letter code) are the minimal peptide sequence to model both the coordination mode and catalytic cycle of NiSOD enzymes.[23,28–31] It was also demonstrated that model complexes are capable of assisting the decomposition of superoxide anion O_2^- and that the redox cycle also leads to the oxidation of the cysteine residues.

In our previous works, detailed equilibrium, spectroscopic and catalytic activities were reported on nickel complexes formed with NiSOD related peptides.[30,32,33] Our results and previous literature studies confirmed the essential role of both cysteine residues in the dismutation of superoxide ion.[34,35] The combined application of pH-potentiometry with spectroscopic methods revealed that the cysteine residue in the second position of the peptide chain is crucial to induce spin pairing of nickel(II), while the distant cysteine affects the redox potential of the Ni(II)/Ni(III) couple.[32] We have also studied the coordination ability and catalytic features of multiple NiSOD binding loops and oxidation of the cysteine residues was observed similarly to those reported earlier. The results revealed that the binuclear nickel complex exhibits superior SOD activity, the Ni(III) species rapidly accumulates and is removed through a fast degradation process; consequently, the nickel assisted catalysis ceases.[33] The oxidative stability of a set of NiSOD related metallopeptides was studied and correlated with their catalytic activities.[36] It was confirmed by stopped-flow kinetic method that one of the key factors is the replacement of carboxamide group for secondary amine in the nickel coordination sphere. Such an alternation leads to improved catalytic activity and higher sensitivity for oxidation compared to the model metallopeptides investigated in that study.[36] On the basis of these results, it is an intriguing issue how the active form(s) of the catalyst can be stabilized to improve the efficiency in the dismutation of superoxide anion.

In this paper, we report thorough equilibrium, spectroscopic, computational and SOD activity studies on the new metallopeptide containing the NiSOD binding motif (denoted as **wtPen** throughout the text, Scheme 1). Its sequence is H(Pen)DLPCGLY, where the first cysteine was replaced by penicillamine which features two-electrons donating methyl groups. This study demonstrates that both the steric and electronic features of penicillamine may alter the activity of the catalyst during the decomposition of superoxide anion.

Results and discussion

Protonation equilibria of **wtPen** were investigated by using pH-potentiometry and the acid dissociation constants are col-

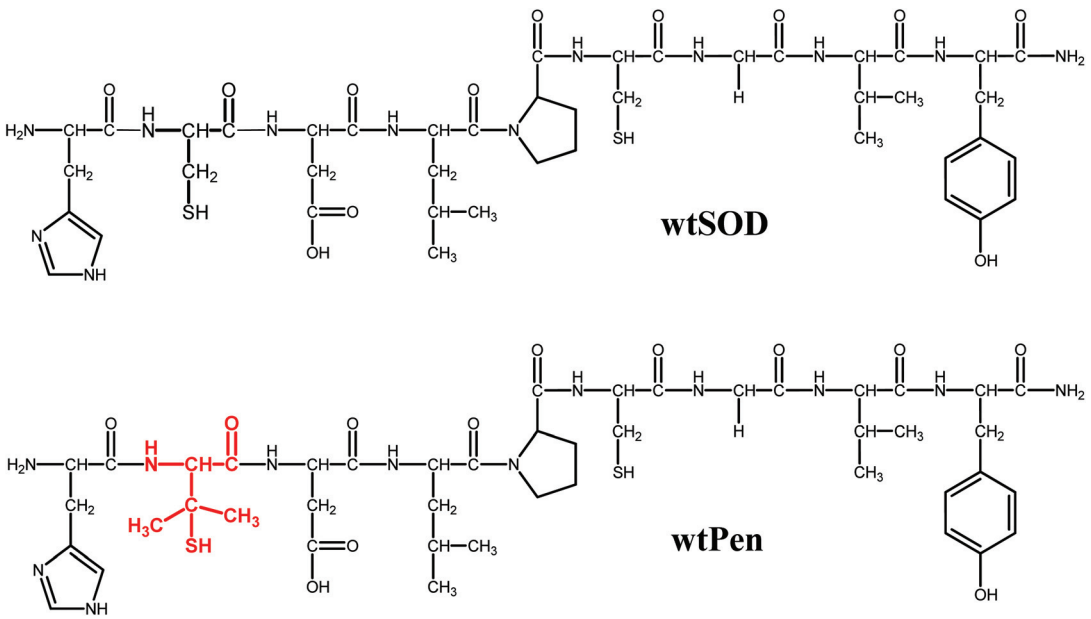

Scheme 1 Structural formulae of the NiSOD binding loop (**wtSOD**) and the peptide investigated in this study (**wtPen**). Mutation on the nonapeptide backbone is highlighted by red color.

Table 1 The stepwise deprotonation constants (log K_i) of the peptides and the equilibrium constants (log K_{pqr}) of the nickel(II) complexes formed with **wtPen** and **wtSOD** (L)[a]

log K_i Species	**wtPen**	**wtSOD**[b]	log K_{pqr}	**wtPen** Species	**wtSOD**[b]
$[H_6L]^{2+}$	3.78(5)	3.58	$[NiH_3L]^{+}$	4.87(2)	4.76
$[H_5L]^{+}$	5.42(7)	5.48	$[NiHL]^{-}$	5.40(1)	5.61
$[H_4L]$	7.09(6)	7.20	$[NiL]^{2-}$	6.86(3)	6.52
$[H_3L]^{-}$	8.26(6)	8.25	$[NiH_{-1}L]^{3-}$	9.89(4)	9.26
$[H_2L]^{2-}$	9.15(6)	8.92	$[NiH_{-2}L]^{4-}$	11.21(5)	
$[HL]^{3-}$	10.07(5)	9.88			
$\sum \log K_i$	43.77	43.31	log $K(N^{-})$[c]	6.86	6.52
Fitted pH range	2.6–11.6		Fitted pH range	3.9–11.3	

[a] 3σ standard deviations are indicated in parentheses. I = 0.2 M KCl, T = 298 K. [b] Data are taken from ref. 30. [c] Equilibrium constant for the deprotonation of amide N. log $K(N^{-})$ = log β(NiHL) − log β(NiL).

lected in Table 1. The protonation processes were also followed by UV-vis spectroscopy which offers the possibility to determine the individual spectra of each species involved in the acid–base processes (Fig. S1–S4†). Details on the acid–base character are reported in the ESI.†

The overall stability constants of the nickel(II)–**wtPen** complexes were obtained by pH-potentiometric method and are reported in Table 1 and Table S1,† while the corresponding concentration distribution of the complexes as a function pH is shown in Fig. 1.

In general, the complex formation processes of **wtPen** show similarities to those reported in the nickel(II)/**wtSOD** system.[30] The complex formation reactions between nickel(II) and the peptide start in the slightly acidic pH range with the $[NiH_3L]^{+}$ species, where L indicate **wtPen**. In this complex, nickel(II) is accommodated by the (NH_2,N_{Im}) donor groups (histamine-like coordination) in an octahedral crystal field. This feature is confirmed by the lack of the *d*–*d* absorption between 400–500 nm in the UV-vis spectra. The equilibrium constant for the formation of histamine-like coordination mode is calculated, log $K_{Histamine}$ = 5.93, which is close to the log K of histamine-like coordination of $[NiH_3L]^{+}$ complex of **wtSOD** (log K = 6.39).[30] The agreement of these stability constants strongly supports the same coordination mode and confirms that the carboxylate group of aspartic acid residue – which is already deprotonated in this pH range – does not have any significant contribution to the metal binding.

Upon increasing the pH, a further base consumption process yields the $[NiHL]^{-}$ complex, while the formation of $[NiH_2L]$ can be excluded on the basis of pH-potentiometric data, Fig. S1.† The formation of $[NiHL]^{-}$ exhibits cooperative feature and is accompanied by characteristic changes both in the CD and UV-vis spectra (Fig. 2 and Fig. S5†). An intense band was observed in the UV-vis spectra at 465 nm which proves that the complex has a square planar geometry and indicates that the amide nitrogen of the peptide backbone is involved in the metal binding.

In parallel, the CD spectra exhibit a new band at 270 nm. In this wavelength range, the Ni(II)–imidazole and Ni(II)–N^{-} charge transfer bands are characteristic. In addition, the CD

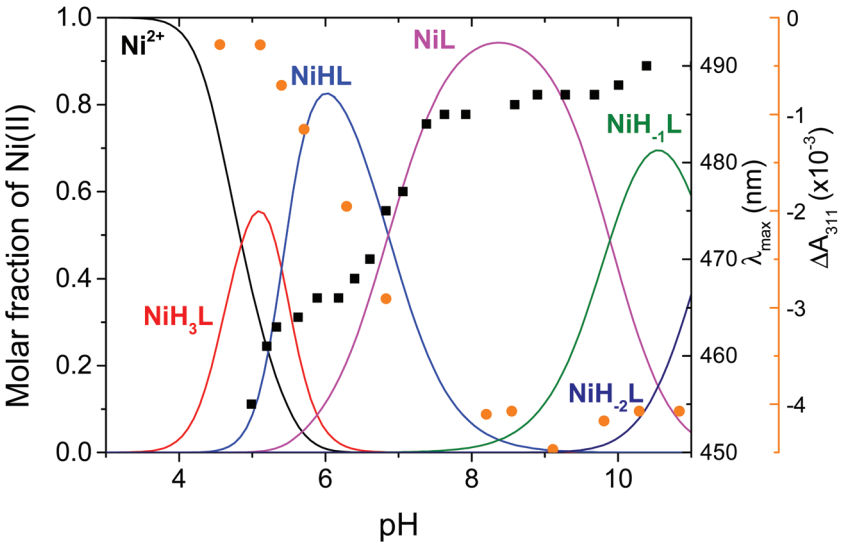

Fig. 1 Concentration distribution of the complexes formed between Ni(II) and **wtPen** (left axis), and the λ_{max} values (■) and ΔA at 311 nm (●) (right axes) as a function of pH at 1 : 1 metal to ligand ratio (I = 0.2 M (KCl), T = 298 K). $c_{Ni(II)}$ = 2 mM.

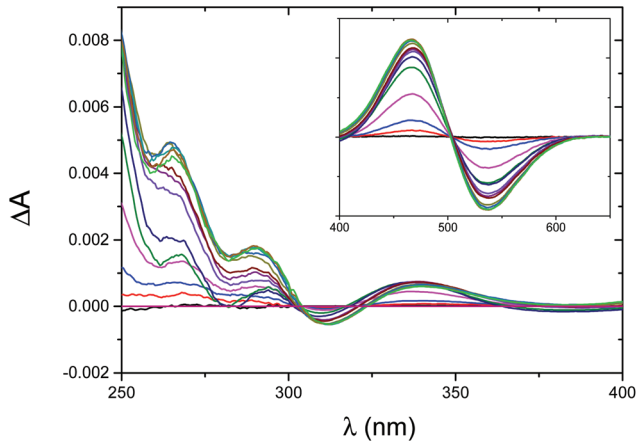

Fig. 2 CD spectra of the Ni(II)/**wtPen** 1 : 1 system as a function of pH. The spectra were recorded between pH 4.56 and 11.58. Inset: Selected part of the *d*–*d* transition. $c_{Ni(II)}$ = 2 mM.

spectra exhibit a band at 330 nm which confirms the binding of one of the thiolate groups. On the basis of the spectroscopic data, the (NH_2,N_{Im},N^-,S^-(Cys)) coordination mode is attributed to $[NiHL]^-$, although a weak axial interaction is expected between the Ni(II) and imidazole-N of histidine (*vide infra*).

This coordination mode features a (5,6)-membered chelate system which is supported by the macrochelation of the distant cysteinyl residue. Additional base consumption process provides the active structure of NiSOD due to the binding of the thiolate group of penicillamine residue. The well resolved CD spectra exhibit a new band at 311 nm with negative Cotton-effect which is a clear evidence for the binding of the penicillamine moiety, *e.g.* D-penicillamine was used in the synthesis and the introduction of methyl substituents of penicillamine results in higher excitation energies than that of cysteine. Such a feature cannot be observed in the UV-vis spectra, these transitions collapse into a single absorption band with maximum at 340 nm. Therefore, the formation of this complex can selectively be followed by CD spectroscopy at 310 nm and the good correlation between ΔA and the species distribution further confirms the proposed coordination mode (Fig. 1). This $[NiL]^{2-}$ complex has a stoichiometry of $NiH_{-1}L(H)$ where the tyrosine residue remains protonated and is dominant at the physiological pH-range. The UV-vis and CD spectra provide further evidence for the formation of (NH_2,N^-,S^-,S^-) coordinated species, although the spectroscopic parameters differ from those observed for the wild-type fragment of NiSOD.[37] This is most probably due to the presence of penicillamine moiety in the coordination sphere which significantly affects the electronic features of the complex. The coordination mode was proved by NMR spectroscopy. In Fig. S6,† the ^1H–^{13}C HSQC spectra are shown in the presence and absence of nickel(II) at pH 7.8. The addition of nickel(II) causes a large shift of several NMR signals. Drastic effect was observed on the methyl groups of penicillamine moiety which is presumably due to the binding of the thiolate group and amide nitrogen of the peptide backbone. In addition, the His-CH_2 signals are affected by the deprotonation and coordination of peptide nitrogen. These results are consistent with the binding of one of the amide nitrogen atoms from the peptide backbone and the thiolate group of penicillamine.

To corroborate the exclusive existence of this complex, ESI-TOF-MS experiments were carried out. The MS spectrum recorded in the Ni(II)/**wtPen** 0.9 : 1 system is shown in Fig. S7.† The major peaks are attributed to the mononuclear nickel(II) complex $[NiL]^{2-}$ ($\equiv[NiH_{-1}L(H)]^{2-}$) with m/z = 543.1789, to the adduct with sodium ($[NiH_{-1}L + Na^+]^{2-}$) with m/z = 554.1699, and to the ligand L^- with m/z = 1031.4450. The good agreement between all of the observed and calculated m/z values supports the existence of the postulated species (Table S2 and Fig. S8†). In addition, the MS spectra do not exhibit any indication for the formation of dimeric or bis-ligand species. Further deprotonation processes lead to the formation of $[NiH_{-1}L]^{3-}$ and $[NiH_{-2}L]^{4-}$ complexes. Since these species are relevant in strongly alkaline solutions only, their complex formation equilibria are discussed in the ESI, Fig. S9.†

The structure, the effect of the metal binding on the peptide conformation and the electronic absorption spectrum of the major complex present under physiological pH in the Ni(II)/**wtPen** system, $[NiL]^{2-}$ ($\equiv[NiH_{-1}L(H)]^{2-}$), were elucidated with a multistep modelling strategy. The results were compared with those obtained for similar species of **wtSOD**. The approach consisted in: (i) build a starting model for both the metal free and mononuclear Ni(II)–**wtSOD** and Ni(II)–**wtPen** peptide fragments (a.a. 1–9) based on the X-ray structure of Ni(II)–SOD; (ii) carry out a MD simulation in order to find their most stable conformation in solution and elucidate the effect of Ni(II) coordination on the folding; (iii) optimise such conformation at full-DFT theory level; and (iv) predict its electronic vertical transitions comparing the results with the experimental bands.

The metal free peptides display the behaviour of typical intrinsically disordered peptides with continuous transition between folded and unfolded states with a main extended conformation. Upon Ni(II) coordination, the metal induces a significant loss of flexibility. Cluster analysis performed on the full length MD experiments shows one predominant conformation in which the square planar Ni(II) coordination geometry is highly retained and a mainly α-helix conformation is adopted by residues 3–9. Overall, the results highlight that both models are stable during 200 ns of the MD and thus they were selected for subsequent DFT analysis. The representative frames of the most sampled conformations for **wtSOD** (the native fragment of NiSOD without metal coordination), Ni(II)–**wtSOD** and Ni(II)–**wtPen** species are reported in Fig. 3a–c. It is plausible that, after the deprotonation of first peptide-NH and SH of Pen and Cys, the interaction of N_{Im} changes from an equatorial to an axial position.

DFT optimization of the structures confirms the square planar Ni(II) coordination geometry with no binding of N_{Im} of His residue. The final Ni(II)–donor bond lengths are: Ni–NH_2 is 2.007 Å (2.008 Å for **wtSOD**), Ni–N^- 1.895 Å (1.901 Å), Ni–

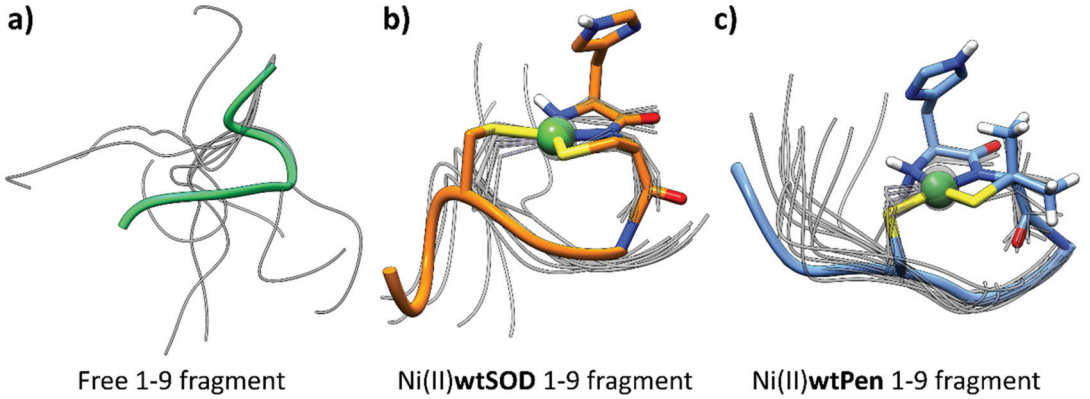

Fig. 3 Representative structures for the most populated clusters obtained along the 200 ns MD for: (a) **wt** (green backbone); (b) Ni(II)–**wtSOD** (orange backbone); and (c) Ni(II)–**wtPen** (blue backbone) fragments together with the most representative frames of other identified clusters. The stoichiometry of the Ni(II) species is $[NiL]^{2-}$ ($\equiv[NiH_{-1}L(H)]^{2-}$) with ($NH_2$, N^-, S^-, S^-) coordination.

S_{Pen2}^- 2.190 Å (Ni–S_{Cys2}^- 2.213 Å), Ni–S_{Cys6}^- 2.250 Å (2.261 Å), while the apical Ni–N_{His1} distance is very long, 4.168 Å (4.129 Å). The Cartesian coordinates of the corresponding complexes are collected in Tables S3 and S4.† Noticeably, the introduction of penicillamine moiety results in a shorter bond distance between nickel(II) and the thiolate group in second position than that calculated for **wtSOD**.

The predicted spectra at TD-DFT theory level are qualitatively in agreement with the experimental results at physiological pH for $[NiL]^{2-}$. In the case of Ni(II)–**wtPen**, the principal fitted bands display their maxima between 332 and 502 nm, composed by clear *d–d* transitions from internal occupied MOs with metal character to the Ni-$d_{x^2-y^2}$ LUMO orbital. The two intense transitions around 300 nm are assigned to metal-to-ligand or ligand-to-metal charge transfers (MLCT and LMCT). The analysis and the list of the calculated vertical transitions for the $[NiL]^{2-}$ species formed in the Ni(II)/**wtPen** and Ni(II)/**wtSOD** systems are reported in Tables S5 and S6 of the ESI.†

Cyclic voltammetry (CV) and differential pulse voltammetry (DPV) were used to obtain electrochemical data of the Ni(II)-**wtPen** and Ni(II)-**wtSOD** complexes at pH 7.6 (Fig. S10†). The cyclic voltammogram shows irreversible feature for these species (the anodic peak occurs at 0.591 V and 0.428 V *versus* Ag/AgCl for Ni(II)-**wtPen** and Ni(II)-**wtSOD**, respectively). The anodic peaks clearly confirm that the two complexes show somewhat different redox properties.

The formation of nickel(III) transient species was followed by EPR spectroscopy. KO_2 stabilized in 18-crown-6 was used as an agent to oxidize *in situ* the corresponding nickel(II) complexes. The EPR spectra are shown in Fig. 4 and the spin-Hamiltonian parameters are collected in Table S7.†

The EPR spectra unambiguously prove that the oxidation of nickel(II) occurs, and the unpaired electron is located in the d_{z^2} orbital resulting in a $g_x \sim g_y > g_z \sim g_e$ relationship between the g values.[38,39] The interaction between the unpaired electron of nickel(III) and one nitrogen donor with nuclear spin $I = 1$ yields a three-band superhyperfine splitting centered around $g \sim 2$.

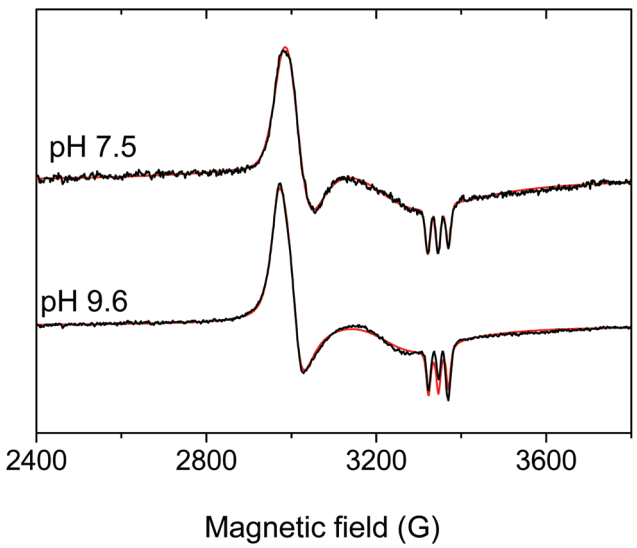

Fig. 4 X-band EPR spectra recorded at 77 K in the Ni(II)/**wtPen** system after *in situ* oxidation (black) and the simulated EPR spectra (red).

Although such square pyramidal coordination environment features the oxidized form of wild-type fragment of NiSOD,[28,30] the EPR parameters of **wtPen** differ.

To predict the conformation of the metallopeptides and the spin Hamiltonian EPR parameters of monomeric Ni(III)–**wtSOD** and Ni(III)–**wtPen** complexes, a computational protocol similar to that described for the nickel(II) complexes was followed (*vide infra*). The $\boldsymbol{g}$ and $\boldsymbol{A}$ tensors of ^{63}Ni and ^{14}N nuclei were computed with the functional BP and basis set 6-311 g(d, p) after a validation on a small benchmark consisting of four square planar, square pyramidal and octahedral Ni(III) complexes formed by maleonitriledithiolato, *N*,*N*′-disalicylidene-4,5-dichloro-1,2-phenylenediamine and pyridine ligands (see Tables S8–S12†). MD analyses unveil stable square pyramidal Ni(III) coordination geometry and, particularly for Ni(III)–**wtPen**, more flexible structures from mainly folded to extended

conformations of the residues 3–9. The representative frames of the most sampled conformation for Ni(III)–**wtSOD** and Ni(III)–**wtPen** are reported in Fig. S11† and their Cartesian coordinates are summarized in Tables S13–S16.†

Considering the flexibility displayed by the oxidized form of the metallated peptides, the fast oxidation times and by analysing the most sampled conformations, the α-helix folding derived from the previous simulations was also selected for DFT analysis.

The energy order of the Ni-based MOs, Ni-d_{xy} ~ Ni-d_{xz} ~ Ni-d_{yz} < Ni-d_{z^2} < Ni-$d_{x^2-y^2}$, agrees well with the prediction of the ligand field theory.[40] Analysis of the MOs composition and spin density shows that the unpaired electron is mainly on the Ni-d_{z^2} orbital, in line with the order of the g values (see Table S7†). This MO is shown in Fig. S12 of the ESI.†

On the optimized structures, the spin Hamiltonian parameters were computed and compared with the EPR experimental results (Table 2). The highest spin density was found on the Ni atom confirming the Ni(III) oxidation state. Moreover, the equatorial nitrogen donors, NH_2 and N^-, display negligible contribution to the superhyperfine constant A_z^N, in line with literature results for other Cu(II)[41] and Ni(III) complexes.[42–46] Therefore, the superhyperfine resonances observed in the EPR spectra (Fig. 4) with **wtPen** were attributed to the axial N_{im} of His1 residue. Such an observation for Ni(III) can be explained assuming that the delocalisation of the spin density to the imidazole ring occurs through the MO that describes the coordinative bond formed by Ni-d_{z^2} and sp^2 orbital on N_{Im}. This reinforces the finding that for such systems the unpaired electron is located on Ni-d_{z^2} orbital. In contrast, the delocalization on the coordinated equatorial nitrogens is not possible and the spin density on them is almost negligible. This accounts for the small, lower than 3×10^{-4} cm^{-1} values of A^N in these systems. Analysis of the total spin density (α–β) shows that the unpaired electron is localized on Ni and N_{Im} atoms (Fig. 5).

The comparison of the experimental and the computed spin Hamiltonian parameters (Table 2) indicates that α-helix folding state is retained in the transient Ni(III) species. In fact, the deviations from the experimental values are huge for the extended conformations (~50%), suggesting that no fast conformational changes are induced upon the $1e^-$ oxidation process. The coordination environment around Ni(III) is square

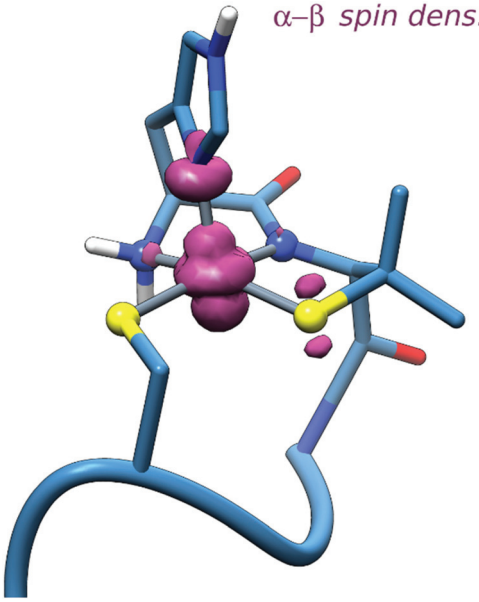

Fig. 5 Total (α–β) spin density (isovalue: 0.007) plot for Ni(III)-**wtPen** species computed for the DFT energy minimum.

pyramidal. In contrast with Ni(II), the axial interaction with N_{Im} of His1 residue is strong with bond lengths of 2.075 and 2.073 Å for **wtPen** and **wtSOD**. The other distances in the DFT optimized structures are: Ni–NH_2 is 2.033 Å (2.034 Å for **wtSOD**), Ni–N^- 1.934 Å (1.934 Å), Ni–S_{Pen2}^- 2.203 Å (2.220 Å), and Ni–S_{Cys6}^- 2.281 Å (2.277 Å). The optimized geometries accounting for the experimental EPR parameters are reported in Fig. 6.

In a dedicated stopped-flow experiment, the Ni(II)-**wtPen** complex was mixed with KO_2 in DMSO to produce the corresponding Ni(III) complex. The progress of the reaction was monitored in a stopped-flow experiment using the PDA detector which offers a possibility to record the electronic absorption spectra of the species. Mixing the Ni(II)-wtPen complex with equimolar KO_2 solution rapidly yields the corresponding Ni(III) complex which exhibits characteristic absorption at around 385 nm that is assigned to S/N(π) → Ni(d_π*) charge transfer band according to earlier literature data (Fig. S13†).[47] Since only a few studies are reported on the electronic absorp-

Table 2 Comparison of values of selected experimental and calculated spin Hamiltonian parameters. Computations were made at BP DFT theory level[a,b]

Species (folding)	$A_z^{N exptl\ b,c}$	$A_z^{N calcd\ b,d}$	g_x^{exptl}	$g_x^{calcd\ e}$	g_y^{exptl}	$g_y^{calcd\ e}$	g_z^{exptl}	$g_z^{calcd\ e}$
Ni(III)–**wtSOD** (extended)[f]	23.7	11.6 (−51.1)	2.289	2.148 (−6.2)	2.220	2.124 (−4.3)	2.012	2.020 (0.4)
Ni(III)–**wtSOD** (α-helix)[g]		23.9 (0.8)		2.165 (−5.4)		2.151 (−3.1)		2.019 (0.3)
Ni(III)–**wtPen** (extended)[f]	22.1	12.0 (−45.7)	2.257	2.164 (−4.1)	2.251	2.142 (−4.8)	2.013	2.020 (0.3)
Ni(III)–**wtPen** (α-helix)[g]		23.4 (5.9)		2.164 (−4.1)		2.150 (−4.5)		2.020 (0.3)

[a] Calculations carried out at BP/6-311 g(d,p) theory level with ORCA 4.0 (see ESI† for selection of the method). [b] Value in 10^{-4}·cm^{-1}. [c] A_z^N for the axial His1-N donor. [d] Percent deviation in parenthesis, calculated as $[(A_z^{Ncalcd} - A_z^{Nexptl})/A_z^{Nexptl}] \times 100$. [e] Percent deviation calculated as $[(g_i^{calcd} - g_i^{exptl})/g_i^{exptl}] \times 100$ with $i = x, y, z$. [f] Representative structure of the most populated cluster. [g] α-Helix structure optimized from the Ni(II) MDs.

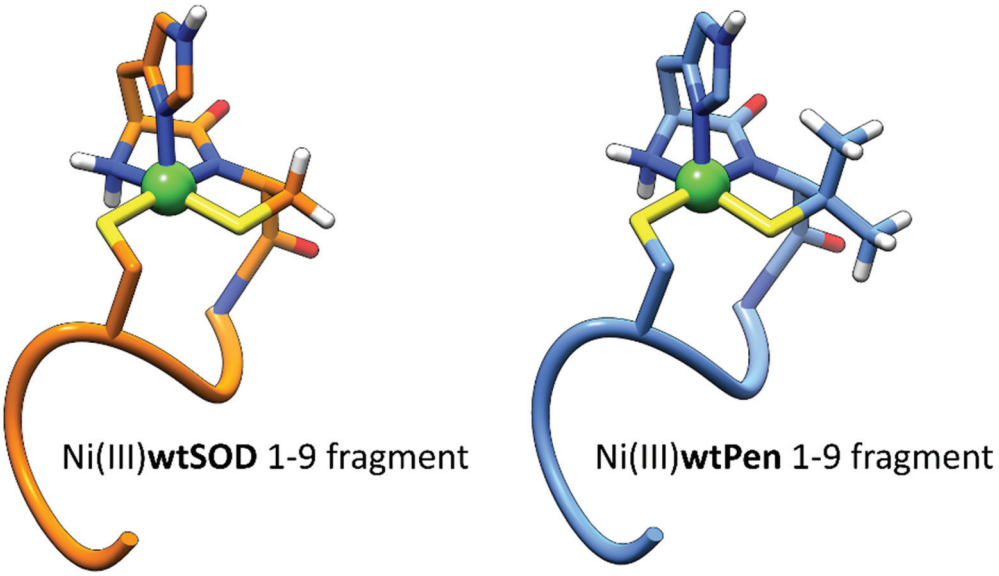

Fig. 6 DFT optimized conformations (B97D) accounting for the experimental EPR parameters of Ni(III)–**wtSOD** (left, orange backbone) and Ni(III)–**wtPen** (right, blue backbone).

tion spectra of Ni(III) complexes, the MO's involved in the transitions were analysed by further TD-DFT calculations. The principal fitted band displays a maximum at around 340 nm in good agreement with the experimental observations. It is composed by several LMCT transitions with the most intense involving one-electron promotion from internal occupied MOs mainly localized on His1, Cys6 and Asp3 residues to the Ni-$d_{x^2-y^2}$ based LUMO or LUMO+1 orbitals. Other LMCT transitions involve excitations with main $L_{His1/Asp3/Cys6/Tyr9} \rightarrow$ Ni-$d_{x^2-y^2}$ character (see Table S17†).

Stability of the metallopeptides

Earlier studies indicated that the addition of KO_2, O_2 or H_2O_2 to the reduced form of metallopeptides leads to substantial sulfur-based oxidation processes yielding sulfenate, sulfinate, sulfonate, cysteine-*S*-monoxide or cysteine-*S*-dioxide products.[36,48] The Ni(II)-**wtPen** and **wtSOD** complexes remain intact when they are exposed to air for 12 hours. In contrast, drastic changes were observed in the UV-Vis spectra of these species upon the addition of one H_2O_2 equivalent (Fig. S14†). However, this degradation process occurs on a much longer time scale than the catalytic dismutation reaction.

Catalytic activity

The SOD activity of the nickel complex of **wtPen** was studied by monitoring the decay of the superoxide anion at 260 nm in water/DMSO 1 : 1 solvent mixture and the results were compared with those obtained for the nickel complex of **wtSOD**. Sequential stopped-flow measurements were used to avoid the spectral disturbances. Details of the experimental protocol are reported in our previous paper.[33]

First, the spontaneous decomposition of the superoxide anion was investigated in the absence of catalyst. Moreover, the initial absorbance of the kinetic traces allows us to determine the concentration of superoxide anion after the incubation time (40 s). A simple second-order decay was observed in the spontaneous decomposition of superoxide anion and the second order rate constant, $k_1 = (3.84 \pm 0.03) \times 10^4\ M^{-1}\ s^{-1}$, is in excellent agreement with that reported earlier.[49]

In the presence of the NiSOD mimic, the absorbance drops very fast from its initial value (*ca.* 0.5) to below 0.3 in the first measured point (at 2 ms) of the kinetic traces. This proves that a substantial part (40%) of the reaction proceeds within the dead-time of the instrument (*ca.* 1.5 ms). Since the non-catalyzed decay of superoxide occurs on considerably longer timescale, these results unambiguously prove that the nickel complex of **wtPen** exhibits superior SOD activity. Unfortunately, the kinetic traces cannot be fitted with a simple first-order expression assuming steady-state conditions for the Ni^{III} complex. In reality, the absorbance steadily changes in a slow process, that can only be explained by considering that the nickel assisted dismutation of superoxide kinetically couples with the degradation of the complex. The postulated reaction scheme is shown in Scheme S1.† The model incorporates the spontaneous decomposition of the superoxide anion (k_1), the dismutation cycle (k_2, k_3) and the degradation of the Ni^{III} complex (k_4). Since the Ni^{II} complex is stable in the absence of oxidant, it is reasonable to assume that the degradation occurs in the Ni^{III} complex. In this species, Ni^{III} may be reduced in an intramolecular redox step, and the nickel assisted dismutation ceases yielding an unidentified nickel complex (Ni*). The kinetic model includes reactions (1)–(4) and the corresponding differential equation system is given by eqn (5)–(9).

$$2H^+ + 2O_2^- \rightarrow H_2O_2 + O_2 \quad k_1 \qquad (1)$$

$$Ni^{II}L + 2H^+ + O_2^- \rightarrow Ni^{III}L + H_2O_2 \quad k_2 \tag{2}$$

$$Ni^{III}L + O_2^- \rightarrow Ni^{II}L + O_2 \quad k_3 \tag{3}$$

$$Ni^{III}L \rightarrow Ni * L \quad k_4 \tag{4}$$

$$\frac{d[O_2^-]}{dt} = -k_1 \times [O_2^-]^2 - k_2 \times [Ni^{II}L][O_2^-] - k_3 \times [Ni^{III}L][O_2^-] \tag{5}$$

$$\frac{d[H_2O_2]}{dt} = k_2 \times [Ni^{II}L][O_2^-] \tag{6}$$

$$\frac{d[Ni^{II}L]}{dt} = -k_2 \times [Ni^{II}L][O_2^-] + k_3 \times [Ni^{III}L][O_2^-] \tag{7}$$

$$\frac{d[Ni^{III}L]}{dt} = k_2 \times [Ni^{II}L][O_2^-] - k_3 \times [Ni^{III}L][O_2^-] - k_4 \times [Ni^* L] \tag{8}$$

$$\frac{d[Ni^* L]}{dt} = k_4 \times [Ni^{III}L] \tag{9}$$

The experimental data were evaluated by fitting the absorbance of each kinetic trace (at 260 and 376 nm) on the basis of this differential equation system by using a non-linear least-squares approach.[50] At 260 nm, there are several absorbing species, and the absorbance is expressed by eqn (10):

$$Abs = \varepsilon_{Ni(II)} \times [Ni^{II}L] + \varepsilon_{Ni(III)} \times [Ni^{III}L] + \varepsilon_{Ni^*} \times [Ni^*L] + \varepsilon_{O_2^-} \times [O_2^-] + \varepsilon_{H_2O_2} \times [H_2O_2] \tag{10}$$

The kinetic traces were also evaluated at 376 nm where the spectral contribution of superoxide anion is negligible, and the absorbance is expressed by eqn (11):

$$Abs = \varepsilon_{Ni(II)} \times [Ni^{II}L] + \varepsilon_{Ni(III)} \times [Ni^{III}L] + \varepsilon_{Ni*} \times [Ni * L] \tag{11}$$

Since the intramolecular redox degradation (eqn (4)) significantly affects the dismutation cycle, the process was independently examined at comparable concentrations of the catalyst and superoxide anion at 260 and 376 nm using constant complex concentration. Under such conditions, the pseudo-first order approach is not applicable for reactions (2) and (3). The corresponding kinetic traces are shown in Fig. 7 and Fig. S15.†

Evaluation of the data yields the first-order rate constant for the degradation of the Ni^{III} complex, $k_4 = 292 \pm 2\ s^{-1}$ and the molar absorptivities of Ni^{III} and Ni* complexes at 260 nm, $\varepsilon_{Ni(III)} = (2.58 \pm 0.02) \times 10^4\ M^{-1}\ cm^{-1}$, $\varepsilon_{Ni^*} = (1.57 \pm 0.06) \times 10^4\ M^{-1}\ cm^{-1}$, respectively. Noticeably, the estimated first-order rate constants at 260 and 374 nm show excellent agreement supporting the postulated kinetic model. In the final fitting process, k_3 was allowed to float, while k_2 was fixed at $3 \times 10^8\ M^{-1}\ s^{-1}$ and k_1 as well as the molar absorptivities of the $Ni^{II/III}$ and Ni* complexes, O_2^- and H_2O_2 were involved with fixed values obtained from independent experiments. The strong cross-correlation between k_2 and k_3 does not allow simultaneous fitting of these parameters. However, the best fit (*e.g.* considering the smallest standard deviation) was observed when k_2 was fixed at $3 \times 10^8\ M^{-1}\ s^{-1}$ or higher. Below this threshold, unrealistic results were obtained. The same experimental and evaluation protocol were used for **wtSOD** (Fig. S16†), when simultaneous fitting of k_2 and k_3 was feasible. The results are collected in Table 3 and the corresponding kinetic traces are shown in Fig. 8.

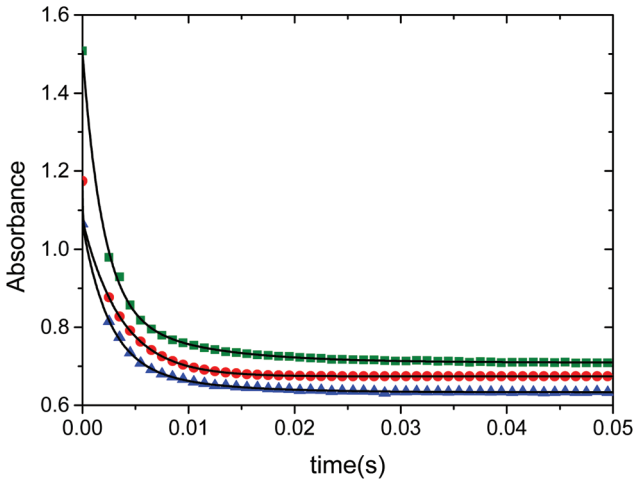

Fig. 7 Kinetic traces recorded in the presence of Ni-**wtPen** complex at comparable concentrations of superoxide anion. $c(complex)^0 = 0.2$ mM; $c(O_2^-)^0 = 0.41$ mM (blue), 0.62 mM (red) and 1.24 mM (green). Solid lines represent the fitted kinetic traces on the basis of the proposed kinetic model. The experiments were carried out in a 1 : 1 aqueous HEPES buffer (50 mM, pH 7.6)/DMSO solvent mixture. $\lambda = 260$ nm, $l = 2$ mm.

It needs to be emphasized that most of the fitted parameters are expected to be pH dependent, therefore the reported values are applicable only at pH 7.6 in water (50 mM HEPES)/DMSO 1 : 1 solvent mixture. Developing a more appropriate kinetic model for the enzyme activity under biological conditions would require experiments in aqueous solution instead of water/DMSO mixture and the use of a much broader concentration range of the reactants. However, experimental limitations prevent such studies. Most prominently, the preparation of stable aqueous O_2^- is not feasible. In spite of the noted shortcomings, the results presented here offer an excellent possibility for comparing the SOD activities of the NiSOD models.

Table 3 Kinetic parameters resulting from the global fitting of the kinetic data

Parameter	**wtPen** Value	**wtSOD** Value	Unit
k_1	$(3.84 \pm 0.03) \times 10^4$	$(3.84 \pm 0.03) \times 10^4$	$M^{-1}\ s^{-1}$
k_2	$>3.0 \times 10^8$	$(9.6 \pm 0.3) \times 10^7$	$M^{-1}\ s^{-1}$
k_3	$(3.15 \pm 0.04) \times 10^7$	$(1.72 \pm 0.08) \times 10^8$	$M^{-1}\ s^{-1}$
k_4	292 ± 2	258 ± 2	s^{-1}
$\varepsilon_{Ni(II)}$	$(1.99 \pm 0.02) \times 10^4$	$(1.48 \pm 0.06) \times 10^4$	$M^{-1}\ cm^{-1}$
$\varepsilon_{Ni(III)}$	$(2.58 \pm 0.02) \times 10^4$	$(2.44 \pm 0.09) \times 10^4$	$M^{-1}\ cm^{-1}$
ε_{Ni^*}	$(1.57 \pm 0.06) \times 10^4$	$(1.8 \pm 0.1) \times 10^4$	$M^{-1}\ cm^{-1}$
$\varepsilon_{O_2^-}$	2686	2686	$M^{-1}\ cm^{-1}$
$\varepsilon_{H_2O_2}$	38	38	$M^{-1}\ cm^{-1}$

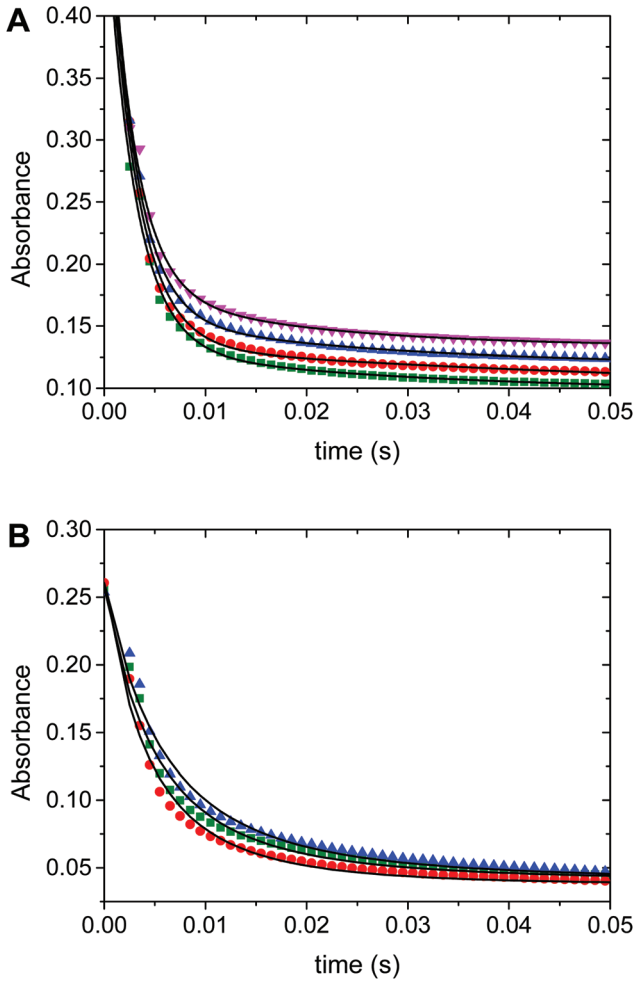

Fig. 8 The decomposition of superoxide anion in the presence of Ni-**wtPen** complexes (magenta: 4.8 μM, blue: 6.3 μM, red: 9.7 μM, green: 19.4 μM) (A) and Ni-**wtSOD** complexes (blue: 2.6 μM, green: 1.2 μM, red: 0.2 μM) (B). Solid lines represent the fitted kinetic traces on the basis of the proposed kinetic model. The experiments were carried out in a 1 : 1 aqueous HEPES buffer (50 mM, pH 7.6)/DMSO solvent mixture. λ = 260 nm, l = 2 mm.

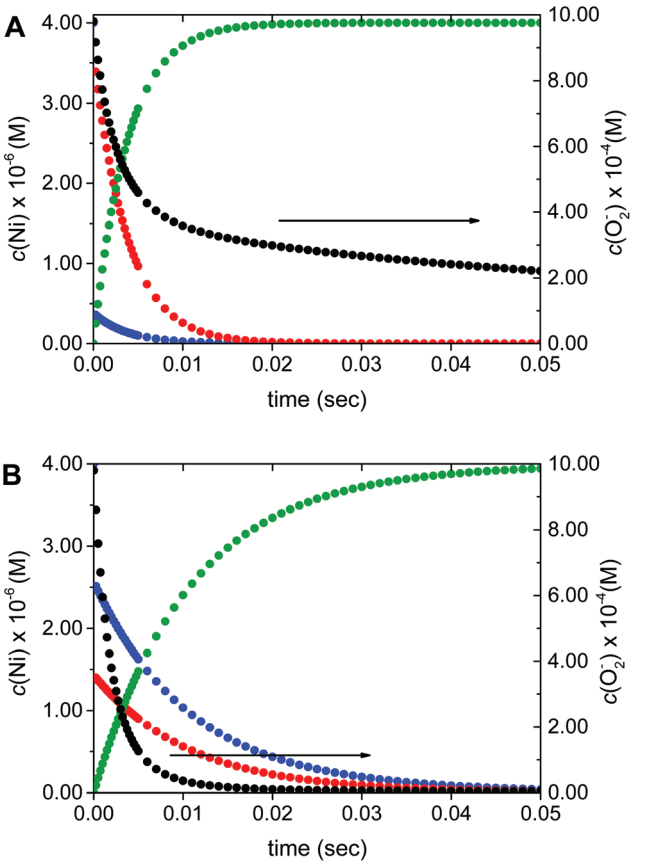

Fig. 9 Calculated concentration profiles of each species as a function of time during the decomposition of superoxide anion in the presence of the catalyst (L refers to **wtPen** (A) and **wtSOD** (B)). Blue: $Ni^{II}L$, red: $Ni^{III}L$, green: Ni*L (left axis); black: O_2^- (right axis). $c(Ni^{II}L)^0$ = 4 μM, $c(O_2^-)^0$ = 980 μM.

Fig. 9 demonstrates how the concentration of each species varies during the dismutation process. For **wtPen**, the results clearly show that the oxidation of nickel(II) (k_2) is considerably faster than the reduction of the corresponding nickel(III) complex (k_3). Therefore, the nickel(III) complex rapidly accumulates after the initiation of the reaction. During this period of time, a substantial amount of the superoxide anion undergoes dismutation (*ca.* 80%) but eventually the decay of the O_2^- concentration becomes considerably slower. In contrast, oxidation of the nickel(II) complex of **wtSOD** is slower than the reduction process, thus the Ni^{II} form is always in excess over the oxidized form. This kinetic feature yields a more effective catalytic activity than that observed for the **wtPen**. The results unambiguously show that the presence of electron donating methyl substituents stabilizes the nickel(III) species which makes the dismutation less favorable.

The results confirm that the disproportionation of the superoxide anion can be controlled by modifying the active site of the catalyst. Unfortunately, the formation of the nickel(III) complex is followed by intramolecular redox degradation yielding the unidentified Ni* species and, consequently, the active form of the catalyst is removed.

Conclusion

Modification on the peptide sequence of NiSOD binding loop by using the natural decomposition product of the antibiotic penicillin yields a new metallopeptide containing D-penicillamine moiety. The excellent metal binding ability is due to the coordination of (NH_2,N^-,S_{Pen2}^-,S_{Cys6}^-) donor set which corresponds to the coordination environment in the reduced form of NiSOD enzyme. Oxidation of the Ni(II) complex yields a Ni(III) species with a stable square pyramidal coordination mode which is due to the binding of the apical histidine and α-helix folding state. Both the EPR parameters and superhyperfine resonances were analyzed by DFT compu-

tations and the results confirmed that the unpaired electron is localized on Ni and N_{Im} atoms.

The metallopeptide exhibits superior catalytic activity in the decomposition of superoxide anion. The decomposition reaction was studied both under catalytic and second-order conditions. This kinetic approach made possible to establish a multi-step kinetic model which incorporates the decomposition of the superoxide anion, the dismutation cycle and the degradation of the catalyst. We unequivocally confirmed that the metallopeptide efficiently catalyzes the dismutation process, and that the Ni^{III} form undergoes redox self-degradation. This side-reaction significantly alters the interpretation of dismutation activity of NiSOD related metallopeptides. The concentration profiles as a function of time clearly show that the superoxide anion is quickly dismutated in the presence of the catalysts. Simultaneous intramolecular redox decomposition of the Ni(III) form of the catalyst eventually ceases the dismutation process.

Earlier studies have reported contradictory conclusions on the role of axial ligands and the hydrogen bond system surrounding the catalytically active center of NiSOD models. It has been proposed that the axial coordination of histidine moieties is not required in the metal assisted degradation of superoxide, *i.e.* an alternative degradation process might exist in the absence of an apical donor group.[36] However, it has also been demonstrated that the presence of an axial ligand in the coordination sphere of nickel(III) enhances the rate of the superoxide disproportionation reaction by affecting the redox activity of the Ni^{II}/Ni^{III} redox couple.[23] Buntkowsky *et al.* have demonstrated that the hydrogen bond network orients the imidazole ring of histidine and helps the stabilization of the Ni(III) oxidation state.[36] Other authors suggested that the hydrogen bonds protect the sulfur atoms of cysteine moieties and enhance the robustness of these groups against oxidative damage of O_2 or H_2O_2.[51,52,53] By introducing penicillamine moiety, the formation of hydrogen bond network can be hindered *via* the bulky methyl substituents. The reaction between the Ni-**wtPen** complex and superoxide accumulates the Ni^{III} species which is involved in a fast self degradation process. Therefore, we propose an alternative role of hydrogen bond network which can involve the stabilization of the Ni^{III} oxidation state toward redox degradation processes. This explains the observed kinetic features, suggesting that an alternative superoxide degradation process may proceed *via* a different path in the Ni/**wtPen** system.

Finally, the presence of the penicillamine moiety (*i.e.* the electron donating substituents of methyl groups) close to the catalytic center is capable to increase the life-time of the Ni(III) transient species. However, the results clearly show that the following features have to be controlled in an effective dismutation reaction: (i) the concentration of the Ni(III) species needs to be kept at relatively low concentration, (ii) the intramolecular redox degradation process needs to be prevented. Further protein designing may solve these issues.

Experimental and computational section

Equilibrium studies

The protonation constants ($\log K_i$) of the ligands and the overall stability constants ($\log \beta_{pqr}$) were determined by pH-potentiometric titration method. The pH reading was converted to hydrogen ion concentration as described by Irving *et al.*[54] Protonation constants and the overall stability constants, $\beta_{pqr} = [Ni_pH_qL_r]/[Ni]^p[H]^q[L]^r$ of the nickel(II) complexes were calculated by using the computational programs, SUPERQUAD[55] and PSEQUAD.[56]

Spectroscopic techniques

UV-visible spectra of the nickel(II) complexes were recorded with an Agilent Technologies Cary 60 UV-VIS spectrophotometer between 200 and 800 nm using the same concentration range as in the pH-potentiometric titrations. The circular dichroism spectra were registered with a Jasco J-810 spectropolarimeter using 1 mm and/or 1 cm cells in the 250–800 nm wavelength range. The individual spectra of the complexes were calculated by solving the overdetermined linear equation system with Matlab on the basis of the estimated stability constants.[57] All CW-EPR spectra were recorded with a BRUKER EleXsys E500 spectrometer. The measured spectra were simulated using the EPR program designated by Rockenbauer and Korecz.[58] Rhombic ***g***-tensor have been used for the simulation of the components. Orientation dependent linewidths were considered. ESI-TOF-MS measurements were carried out with a Bruker maXis II MicroTOF-Q type Qq-TOF-MS instrument (Bruker Daltonik, Bremen, Germany) in negative mode. 1D ^1H and 2D (^1H–^{13}C HSQC) NMR spectra were recorded on a Bruker Avance I 400 spectrometer equipped a BB inverse *z* gradient probe at 298 K.

Computational methods

The molecular modelling approach consisted in a multistep strategy including Molecular Dynamics (MD), Density Functional Theory (DFT) and Time-Dependent-Density Functional Theory (TD-DFT) calculations. (i) The starting models for both the metal free and mononuclear Ni(II)/Ni(III)–**wtSOD** and Ni(II)/Ni(III)–**wtPen** peptide fragments (a.a. 1–9) were obtained from the X-ray structure of Ni(II)–SOD and Ni(III)–SOD (PDB code 1T6U). (ii) MD simulations in TIP3P periodic water box along 200 ns were carried out with OpenMM[66] package in order to find their most stable conformation in solution and elucidate the effect of Ni coordination on the folding. Ni-Bonding force constants and equilibrium parameters were obtained through the Seminario method, using the MCPB.py protocol.[59] The trajectories convergence was assessed by RMSI, RMSF, counting clustering method and PCA analysis.[60] (iii) The most stable conformation was optimized at full-DFT theory level with Gaussian 16 [61] using the functional B97D in continuum model for water. (iv) The UV-vis electronic vertical transitions of the optimized complexes were computed

at TD-DFT theory level using the HSE06 functional in continuum model for water according to the method established previously.[62] (v) For the Ni(III)–**wtSOD** and Ni(III)–**wtPen** peptide fragments the $\boldsymbol{g}$ and $\boldsymbol{A}$ tensors of ^{63}Ni and ^{14}N nuclei were computed through the method implemented into the ORCA package (vers, 4.0),[63,64] with the functional BP.[65] The method was further calibrated in this work toward a dataset of four Ni(III) complexes (Table S8†). All the predicted spectroscopic parameters were compared with the experimental data, either to confirm the conformation of the peptide fragments or to clarify their electronic structure properties. See the ESI† for further technical details.

Electrochemistry

Electrochemical measurements (cyclic voltammetry (CV) and differential pulse voltammetry (DPV)) were performed using a BASI Epsilon Eclipse potentiostat (Bioanalytical Systems Inc., West Lafayette, USA) equipped with a three-electrode arrangement that consists of a platinum wire auxiliary electrode (ALS Co. Japan), a glassy carbon electrode (CHI104) and a Ag/AgCl/3 M KCl reference electrode.

SOD activity measurements

The catalytic activities of the Ni(II) complexes in the decomposition of O_2^- and the formation of Ni(III) transient species and further nickel complexes were studied using an Applied Photophysics SX-20 stopped-flow instrument equipped with a photomultiplier tube as the detector.

Author contributions

The manuscript was written through contributions of all authors. All authors have given approval to the final version of the text.

Conflicts of interest

There are no conflicts to declare.

Acknowledgements

N. L. and I. F. are grateful for the financial support of the Hungarian National Research, Development and Innovation Office (NKFIH PD-128326 and K-124983). The research was also financed by the EU and co-financed by the European Regional Development Fund (under the projects GINOP-2.3.2-15-2016-00008). E. G. and G. S. thank Regione Autonoma della Sardegna (grant RASSR79857) and Fondazione di Sardegna (FdS2017Garribba) for financial support. G.S. also thank Spanish MICINN' Juan de la Cierva program, FJC2019-039135-I. This work is also supported by the ÚNKP-21-4-II New National Excellence Program of the Ministry for Innovation and Technology from the source of the National, Research, Development and Innovation Fund and prepared with the professional support of the Doctoral Student Scholarship Program of the Co-operative Doctoral Program of the Ministry of Innovation and Technology financed from the National Research, Development and Innovation Office.

References

1 I. Khan and M. Waheed Akhtar, Different Approaches For Protein Engineering In Industrial Biotechnology, *Nat. Prec.*, 2011, DOI: 10.1038/npre.2011.5601.1.
2 D. J. Mikolajczak, J. Scholz and B. Koksch, Tuning the Catalytic Activity and Substrate Specificity of Peptide-Nanoparticle Conjugates, *ChemCatChem*, 2018, **10**, 5665–5668.
3 S. P. Godehard, C. P. S. Badenhorst, H. Müller and U. T. Bornscheuer, Protein Engineering for Enhanced Acyltransferase Activity, Substrate Scope, and Selectivity of the Mycobacterium smegmatis Acyltransferase MsAcT, *ACS Catal.*, 2020, **10**, 7552–7562.
4 R. Fasan, Tuning P450 Enzymes as Oxidation Catalysts, *ACS Catal.*, 2012, **2**, 647–666.
5 N. Ma, W. Fang, C. Liu, X. Qin, X. Wang, L. Jin, B. Wang and Z. Cong, Switching an Artificial P450 Peroxygenase into Peroxidase via Mechanism-Guided Protein Engineering, *ACS Catal.*, 2021, **11**, 8449–8455.
6 T. Giraud, S. Bouguet-Bonnet, P. Marchal, G. Pickaert, M.-C. Averlant-Petit and L. Stefan, Improving and fine-tuning the properties of peptide-based hydrogels via incorporation of peptide nucleic acids, *Nanoscale*, 2020, **12**, 19905–19917.
7 P. C. Cirino and F. H. Arnold, Protein engineering of oxygenases for biocatalysis, *Curr. Opin. Chem. Biol.*, 2002, **6**, 130–135.
8 D. R. Boyd, N. D. Sharma and C. C. R. Allen, Aromatic dioxygenases: molecular biocatalysis and applications, *Curr. Opin. Biotechnol.*, 2001, **12**, 564–573.
9 Z. Li, J. B. van Beilen, W. A. Duetz, A. Schmid, A. de Raadt, H. Griengl and B. Witholt, Oxidative biotransformations using oxygenases, *Curr. Opin. Chem. Biol.*, 2002, **6**, 136–144.
10 I. Fridovich, in *Encyclopedia of Biological Chemistry*, ed. M. D. Lane, Elsevier, New York, 2004, pp. 135–138.
11 C. R. Kliment, J. M. Tobolewski, M. L. Manni, R. J. Tan, J. Enghild and T. D. Oury, Extracellular superoxide dismutase protects against matrix degradation of heparan sulfate in the lung, *Antioxid. Redox Signaling*, 2008, **10**, 261–268.
12 S. K. Sah, G. Agrahari and T.-Y. Kim, Insights into superoxide dismutase 3 in regulating biological and functional properties of mesenchymal stem cells, *Cell Biosci.*, 2020, **10**, 22.
13 I. A. Abreu and D. E. Cabelli, Superoxide dismutases—a review of the metal-associated mechanistic variations, *Biochim. Biophys. Acta*, 2010, **1804**, 263–274.
14 Y. Sheng, I. A. Abreu, D. E. Cabelli, M. J. Maroney, A.-F. Miller, M. Teixeira and J. S. Valentine, Superoxide Dismutases and Superoxide Reductases, *Chem. Rev.*, 2014, **114**, 3854–3918.

15 S. W. Ragsdale, Nickel-based Enzyme Systems, *J. Biol. Chem.*, 2009, **284**, 18571–18575.
16 D. M. Kurtz, Microbial Detoxification of Superoxide: The Non-Heme Iron Reductive Paradigm for Combating Oxidative Stress, *Acc. Chem. Res.*, 2004, **37**, 902–908.
17 H. Wiseman and B. Halliwell, Damage to DNA by reactive oxygen and nitrogen species: role in inflammatory disease and progression to cancer, *Biochem. J.*, 1996, **313**, 17–29.
18 T. Nishikawa and E. Araki, Impact of Mitochondrial ROS Production in the Pathogenesis of Diabetes Mellitus and Its Complications, *Antioxid. Redox Signaling*, 2007, **9**, 343–353.
19 P. Newsholme, V. F. Cruzat, K. N. Keane, R. Carlessi and P. I. H. de Bittencourt Jr., Molecular mechanisms of ROS production and oxidative stress in diabetes, *Biochem. J.*, 2016, **473**, 4527–4550.
20 A. Umeno, V. Biju and Y. Yoshida, In vivo ROS production and use of oxidative stress-derived biomarkers to detect the onset of diseases such as Alzheimer's disease, Parkinson's disease, and diabetes, *Free Radical Res.*, 2017, **51**, 413–427.
21 A.-F. Miller, Superoxide dismutases: active sites that save, but a protein that kills, *Curr. Opin. Chem. Biol.*, 2004, **8**, 162–168.
22 H. D. Youn, E. J. Kim, J. H. Roe, Y. C. Hah and S. O. Kang, A novel nickel-containing superoxide dismutase from Streptomyces spp, *Biochem. J.*, 1996, **318**, 889–896.
23 K. P. Neupane, K. Gearty, A. Francis and J. Shearer, Probing Variable Axial Ligation in Nickel Superoxide Dismutase Utilizing Metallopeptide-Based Models: Insight into the Superoxide Disproportionation Mechanism, *J. Am. Chem. Soc.*, 2007, **129**, 14605–14618.
24 M. Schmidt, S. Zahn, M. Carella, O. Ohlenschläger, M. Görlach, E. Kothe and J. Weston, Solution Structure of a Functional Biomimetic and Mechanistic Implications for Nickel Superoxide Dismutases, *ChemBioChem*, 2008, **9**, 2135–2146.
25 J. Domergue, P. Guinard, M. Douillard, J. Pécaut, O. Proux, C. Lebrun, A. Le Goff, P. Maldivi, P. Delangle and C. Duboc, A Bioinspired Ni^{II} Superoxide Dismutase Catalyst Designed on an ATCUN-like Binding Motif, *Inorg. Chem.*, 2021, **60**, 12772–12780.
26 J. Wuerges, J.-W. Lee, Y.-I. Yim, H.-S. Yim, S.-O. Kang and K. D. Carugo, Crystal structure of nickel-containing superoxide dismutase reveals another type of active site, *Proc. Natl. Acad. Sci. U. S. A.*, 2004, **101**, 8569–8574.
27 B. Palenik, B. Brahamsha, F. W. Larimer, M. Land, L. Hauser, P. Chain, J. Lamerdin, W. Regala, E. E. Allen, J. McCarren, I. Paulsen, A. Dufresne, F. Partensky, E. A. Webb and J. Waterbury, The genome of a motile marine *Synechococcus*, *Nature*, 2003, **424**, 1037–1042.
28 J. Shearer and L. M. Long, A Nickel Superoxide Dismutase Maquette That Reproduces the Spectroscopic and Functional Properties of the Metalloenzyme, *Inorg. Chem.*, 2006, **45**, 2358–2360.
29 J. Shearer, Use of a Metallopeptide-Based Mimic Provides Evidence for a Proton-Coupled Electron-Transfer Mechanism for Superoxide Reduction by Nickel-Containing Superoxide Dismutase, *Angew. Chem., Int. Ed.*, 2013, **52**, 2569–2572.
30 N. Lihi, G. Csire, B. Szakács, N. V. May, K. Várnagy, I. Sóvágó and I. Fábián, Stabilization of the Nickel Binding Loop in NiSOD and Related Model Complexes: Thermodynamic and Structural Features, *Inorg. Chem.*, 2019, **58**, 1414–1424.
31 G. Csire, A. Kolozsi, T. Gajda, G. Pappalardo, K. Várnagy, I. Sóvágó, I. Fábián and N. Lihi, The ability of the NiSOD binding loop to chelate zinc(II): the role of the terminal amino group in the enzymatic functions, *Dalton Trans.*, 2019, **48**, 6217–6227.
32 N. Lihi, D. Kelemen, N. V. May and I. Fábián, The Role of the Cysteine Fragments of the Nickel Binding Loop in the Activity of the Ni(II)-Containing SOD Enzyme, *Inorg. Chem.*, 2020, **59**, 4772–4780.
33 D. Kelemen, N. V. May, M. Andrási, A. Gáspár, I. Fábián and N. Lihi, High Enzyme Activity of a Binuclear Nickel Complex Formed with the Binding Loops of the NiSOD Enzyme**, *Chem. – Eur. J.*, 2020, **26**, 16767–16773.
34 V. Pelmenschikov and P. E. M. Siegbahn, Nickel Superoxide Dismutase Reaction Mechanism Studied by Hybrid Density Functional Methods, *J. Am. Chem. Soc.*, 2006, **128**, 7466–7475.
35 J. Shearer, Insight into the Structure and Mechanism of Nickel-Containing Superoxide Dismutase Derived from Peptide-Based Mimics, *Acc. Chem. Res.*, 2014, **47**, 2332–2341.
36 D. Tietze, J. Sartorius, B. Koley Seth, K. Herr, P. Heimer, D. Imhof, D. Mollenhauer and G. Buntkowsky, New insights into the mechanism of nickel superoxide degradation from studies of model peptides, *Sci. Rep.*, 2017, **7**, 17194.
37 A. T. Fiedler, P. A. Bryngelson, M. J. Maroney and T. C. Brunold, Spectroscopic and Computational Studies of Ni Superoxide Dismutase: Electronic Structure Contributions to Enzymatic Function, *J. Am. Chem. Soc.*, 2005, **127**, 5449–5462.
38 W.-Z. Lee, C.-W. Chiang, T.-H. Lin and T.-S. Kuo, A Discrete Five-Coordinate Ni^{III} Complex Resembling the Active Site of the Oxidized Form of Nickel Superoxide Dismutase, *Chem. – Eur. J.*, 2012, **18**, 50–53.
39 E. Garribba and G. Micera, The Determination of the Geometry of Cu(II) Complexes: An EPR Spectroscopy Experiment, *J. Chem. Educ.*, 2006, **83**, 1229–1232.
40 Y. Jean, *Molecular Orbitals of Transition Metal Complexes*, Oxford University Press, Oxford, 2005.
41 B. R. McGarvey, Theory of the Spin Hamiltonian Parameters for Low Spin Cobalt(II) Complexes, *Can. J. Chem.*, 1975, **53**, 2498–2511.
42 E. S. Gore and D. H. Busch, Stable octahedral, low-spin nickel(III) complexes of a tetradentate macrocyclic ligand having saturated nitrogen donors, *Inorg. Chem.*, 1973, **12**, 1–3.
43 J. M. Bemtgen, H. R. Gimpert and A. Von Zelensky, Nickel(III) complexes of 3,9-dimethyl-4,8-diazaundeca-3,8-

diene-2,10-dione dioxime with two axial halide ligands. ESR spectra, electronic spectra, and ligand-exchange kinetics, *Inorg. Chem.*, 1983, **22**, 3576–3580.

44 A. Desideri and J. B. Raynor, Electron spin resonance spectroscopy of some dianiono(1,4,8,11-tetra-azacyclotetradecane)-iron(III) and -nickel(III) salts, *J. Chem. Soc., Dalton Trans.*, 1977, 2051–2054.

45 C. Freire and B. de Castro, Spectroscopic characterisation of electrogenerated nickel(III) species. Complexes with N_2O_2 Schiff-base ligands derived from salicylaldehyde, *J. Chem. Soc., Dalton Trans.*, 1998, 1491–1498.

46 B. De Castro and C. Freire, EPR and electrochemical study of nickel(III) complexes of bis(3,5-dichlorosalicylaldehyde) o-phenylenediimine. Evidence for adduct formation with pyridines, *Inorg. Chem.*, 1990, **29**, 5113–5119.

47 P. A. Stenson, A. Board, A. Marin-Becerra, A. J. Blake, E. S. Davies, C. Wilson, J. McMaster and M. Schröder, Molecular and Electronic Structures of One-Electron Oxidized Ni^{II}–(Dithiosalicylidenediamine) Complexes: Ni^{III}–Thiolate versus Ni^{II}–Thiyl Radical States, *Chem. – Eur. J.*, 2008, **14**, 2564–2576.

48 J. Shearer, Dioxygen and superoxide stability of metallopeptide based mimics of nickel containing superoxide dismutase: The influence of amine/amidate vs. bis-amidate ligation, *J. Inorg. Biochem.*, 2013, **129**, 145–149.

49 B. J. Bolann, H. Henriksen and R. J. Ulvik, Decay kinetics of $O_2^{\cdot-}$ studied by direct spectrophotometry. Interaction with catalytic and non-catalytic substances, *Biochim. Biophys. Acta, Gen. Subj.*, 1992, **1156**, 27–33.

50 *Scientist, version 2.0; Micromath Software*, Salt Lake City, 1995.

51 J. Shearer, K. L. Peck, J. C. Schmitt and K. P. Neupane, Cysteinate Protonation and Water Hydrogen Bonding at the Active-Site of a Nickel Superoxide Dismutase Metallopeptide-Based Mimic: Implications for the Mechanism of Superoxide Reduction, *J. Am. Chem. Soc.*, 2014, **136**, 16009–16022.

52 E. M. Gale, B. S. Narendrapurapu, A. C. Simmonett, H. F. Schaefer and T. C. Harrop, Exploring the Effects of H-Bonding in Synthetic Analogues of Nickel Superoxide Dismutase (Ni-SOD): Experimental and Theoretical Implications for Protection of the Ni–SCys Bond, *Inorg. Chem.*, 2010, **49**, 7080–7096.

53 C. S. Mullins, C. A. Grapperhaus and P. M. Kozlowski, Density functional theory investigations of NiN_2S_2 reactivity as a function of nitrogen donor type and N–H···S hydrogen bonding inspired by nickel-containing superoxide dismutase, *JBIC, J. Biol. Inorg. Chem.*, 2006, **11**, 617–625.

54 H. M. Irving, M. G. Miles and L. D. Pettit, A study of some problems in determining the stoicheiometric proton dissociation constants of complexes by potentiometric titrations using a glass electrode, *Anal. Chim. Acta*, 1967, **38**, 475–488.

55 P. Gans, A. Sabatini and A. Vacca, SUPERQUAD: an improved general program for computation of formation constants from potentiometric data, *J. Chem. Soc., Dalton Trans.*, 1985, 1195–1200.

56 L. Zékány and I. Nagypál, *Computational Methods for the Determination of Formation Constants*, Plenum Press, New York, NY, USA, 1985.

57 T. M. MATLAB and, Statistics Toolbox Release 2012b, Inc, Natick, Massachusetts, United States.

58 A. Rockenbauer and L. Korecz, Automatic computer simulations of ESR spectra, *Appl. Magn. Reson.*, 1996, **10**, 29–43.

59 P. Li and K. M. Merz Jr., MCPB. py: A Python Based Metal Center Parameter Builder, *J. Chem. Inf. Model.*, 2016, **56**, 599–604.

60 G. Sciortino, J.-E. Sánchez-Aparicio, J. Rodríguez-Guerra Pedregal, E. Garribba and J.-D. Maréchal, Computational insight into the interaction of oxaliplatin with insulin, *Metallomics*, 2019, **11**, 765–773.

61 M. J. Frisch, G. W. Trucks, H. B. Schlegel, G. E. Scuseria, M. A. Robb, J. R. Cheeseman, G. Scalmani, V. Barone, B. Mennucci, G. A. Petersson, H. Nakatsuji, M. Caricato, X. Li, H. P. Hratchian, A. F. Izmaylov, J. Bloino, G. Zheng, J. L. Sonnenberg, M. Hada, M. Ehara, K. Toyota, R. Fukuda, J. Hasegawa, M. Ishida, T. Nakajima, Y. Honda, O. Kitao, H. Nakai, T. Vreven, J. A. Montgomery Jr., J. E. Peralta, F. Ogliaro, M. Bearpark, J. J. Heyd, E. Brothers, K. N. Kudin, V. N. Staroverov, T. Keith, R. Kobayashi, J. Normand, K. Raghavachari, A. Rendell, J. C. Burant, S. S. Iyengar, J. Tomasi, M. Cossi, N. Rega, J. M. Millam, M. Klene, J. E. Knox, J. B. Cross, V. Bakken, C. Adamo, J. Jaramillo, R. Gomperts, R. E. Stratmann, O. Yazyev, A. J. Austin, R. Cammi, C. Pomelli, J. W. Ochterski, R. L. Martin, K. Morokuma, V. G. Zakrzewski, G. A. Voth, P. Salvador, J. J. Dannenberg, S. Dapprich, A. D. Daniels, Ö. Farkas, J. B. Foresman, J. V. Ortiz, J. Cioslowski and D. J. Fox, *Gaussian 16, revision B.01*, Gaussian, Inc., Wallingford, CT, 2010.

62 G. Sciortino, N. Lihi, T. Czine, J.-D. Maréchal, A. Lledós and E. Garribba, Accurate prediction of vertical electronic transitions of Ni(II) coordination compounds via time dependent density functional theory, *Int. J. Quantum Chem.*, 2018, **118**, e25655.

63 F. Neese, *ORCA – An Ab Initio, DFT and Semiempirical Program Package, Version 4.0, Max-Planck-Institute for Chemical Energy Conversion*, Mülheim a. d. Ruhr, 2017.

64 F. Neese, Software update: the ORCA program system, version 4.0, *Wiley Interdiscip. Rev.: Comput. Mol. Sci.*, 2017, **8**, e1327.

65 F. Neese, Metal and ligand hyperfine couplings in transition metal complexes: The effect of spin–orbit coupling as studied by coupled perturbed Kohn–Sham theory, *J. Chem. Phys.*, 2003, **118**, 3939–3948.

66 P. Eastman, J. Swails, J. D. Chodera, R. T. McGibbon, Y. Zhao, K. A. Beauchamp, L.-P. Wang, A. C. Simmonett, C. D. Harrigan, C. D. Stern, R. P. Wiewiora, B. R. Brooks and V. S. Pande, OpenMM 7: Rapid Development of High Performance Algorithms for Molecular Dynamics, *PLoS Comput. Biol.*, 2017, **13**, e1005659.

